Research Article

Performance Optimization of Slotted Blades for Low-Specific Speed Centrifugal Pumps

Qidi Ke [iD] **and Lingfeng Tang**

School of Mechanical Engineering, Anhui Polytechnic University, Anhui 241000, Wuhu, China

Correspondence should be addressed to Qidi Ke; 2210110117@stu.ahpu.edu.cn

Centrifugal pumps are widely used for the transport of fluids, but low-specific-speed centrifugal pumps widely have problems with serious backflow and low efficiency. In this paper, a low-specific-speed centrifugal pump with a specific speed of 55 is used as a research object. By combining numerical simulation and orthogonal experiment, the pressure distribution and velocity distribution of the flow channel are analyzed, the priority of each geometric factor for slits on pump performance is determined, the geometric parameter structure of the slotted blade is optimized by entropy weight on TOPSIS, the optimal impeller slit solution is obtained. The results show that with a balance of head and efficiency, the order of influence of the factors is: slit center width $b >$ diameter of slit $D >$ shrinkage ratio of slit $f >$ depth of slit $h >$ deflection angle of slit β. The optimal combination of slit geometry parameters is: slit center width is 3 mm, diameter of the slit is 200 mm, shrinkage ratio of the slit is 0.5, depth of the slit is 6 mm, and the deflection angle of the slit is 20°. Through ANSYS FLUENT simulation and experiment of closed pump experiment system, confirmed that hydraulic performance is improved.

1. Introduction

The low-specific-speed pump has the characteristics of a low flow rate and a high head and is widely used in agricultural irrigation and industrial water supply fields. To improve the performance of low-specific-speed pumps, scholars have done research in various areas [1–3]. De Donno and Thakkar et al. used a genetic algorithm and a multiobjective optimization algorithm to enhance the performance of the centrifugal pump, and the effect is significant [4, 5]. Al-Obaidi and Towsyfyan developed an efficient signal processing method based on envelope spectral analysis, which was used to monitor the vibration characteristics of centrifugal pumps, and after that, they investigated the effect of different operating conditions using different statistical features in a time domain analysis (TDA) and detected and diagnosed the cavitation in centrifugal pumps [6, 7]. Zhang et al. and Zhang et al. proposed and optimized the equations and parameters of 3D blade formation [8, 9]. Bai et al. built a vibration test stand to examine the vibration and stability

of cantilever multistage centrifugal pumps at different flow rates [10]. Feng et al. studied the rotational stall characteristics inside the vane diffuser of a centrifugal pump based on ANSYS CFX [11]. Stel et al. conducted numerical and experimental studies on the motion of air bubbles in the impeller of a centrifugal pump and also used numerical particle tracking methods to evaluate the bubble motion [12]. Namazizadeh et al. studied the effect of adding separator blades and modifying their geometry to optimize the impeller of the centrifugal pump [13]. Liu et al. proposed some very excellent and practical optimization and prediction methods for multipump and mixed-flow pumps [14–16]. Li et al. combine the nondominated sorting genetic algorithm-II (NSGA-II) and a modified technique for order preference by similarity to an ideal solution (TOPSIS) based on the Shannon entropy and explore the optimal design of grooves in axial-flow pumps [17].

The major problem with low-specific-speed centrifugal pumps is the backflow inside the flow channel, which reduces the hydraulic performance [18]. To block partial

backflow, usually use the method of setting the splitter blade. The blade method was originally used in the aviation field, but it has not been well studied in centrifugal pumps. Currently, some scholars have studied the relationship between the shape of the slit vane and the performance of centrifugal pumps by using orthogonal tests, but they are not very comprehensive [19, 20]. Zhang et al. and Wei et al. investigated the effect of slot width on drainage performance [21, 22]. The study found that slot drainage will reduce the head, but it will increase its hydraulic efficiency. Zhang et al. aimed to improve the cavitation performance of centrifugal pumps and proposed a new type of impeller for centrifugal pumps with slots, and this worked well [23].

This paper designs the typical low-specific-speed centrifugal pump with a specific speed of 55, analyzed the reasons for its inefficiency, investigated the effect of slit geometry parameters on the hydraulic performance and internal flow field, and performed a multiobjective optimization. This study provides a reference for improving the hydraulic performance of a low-specific-speed centrifugal pump.

2. Centrifugal Pump Structure Design

2.1. Determination of Structural Parameters. The pump studied in this paper is a low-specific-speed centrifugal pump, and the main design parameters are shown in Table 1.

Design the structure of the centrifugal pump according to the given parameters. Hydraulic design is the first step of the study, and the value of the structural parameters will directly affect the performance of the pump.

(1) Pump inlet diameter and inlet speed

$$D_s = k_s \sqrt[3]{\frac{Q}{n}}, \tag{1}$$

where D_s—inlet diameter (m); Q—inlet speed (m³/h); the value of the coefficient k_s ranges from 4~5, and 4 is taken here. After calculation: $D_s = 85.15$ mm, rounding to 80 mm in accordance with the common caliber. Based on the inlet diameter and flow rate, the selected flow velocity $V_s = 2.76$ m/s.

(2) Pump outlet diameter

The formula is as follows:

$$D_d = k_d \sqrt[3]{\frac{Q}{n}}, \tag{2}$$

where D_d—outlet diameter (m); The value of the coefficient k_d ranges from 3.5~4.5, and 3.5 is taken here. So pump outlet diameter $D_d = 74.5$ mm

(3) Specific speed

$$n_s = \frac{3.65n\sqrt{Q}}{H^{3/4}}, \tag{3}$$

where n_s—specific speed; H—head (m). After calculation: $n_s = 55.407$

(4) Efficiency estimation

Table 1: Main design parameters.

Flow Q (m³/h⁻¹)	Head H (m)	Speed n (r/min)
50	25	1440

The hydraulic efficiency of the pump is calculated according to the following equation:

$$\eta_h \approx 1 + 0.0835 \lg \sqrt[3]{\frac{Q}{n}}. \tag{4}$$

After calculation: $\eta_h = 0.8604$.
The volumetric efficiency is calculated by

$$\eta_v \approx \frac{1}{1 + 0.68 n_s^{-2/3}}. \tag{5}$$

After calculation: $\eta_v = 0.9553$
The mechanical efficiency of the disc friction loss is calculated by the following equation:

$$\eta_m = 1 - 0.07 \frac{1}{(n_s/100)^{7/6}}. \tag{6}$$

After calculation: $\eta_m = 0.8606$.
The total efficiency of the pump is

$$\eta = \eta_m \eta_v \eta_h. \tag{7}$$

After calculation: $\eta = 0.7073$.

2.2. Impeller Size Determination. The structure form of centrifugal pump impeller is mainly semiopen type and closed type. The semiopen impeller has the advantage of easy cleaning and easy forming, therefore, the impeller used in this paper is a semiopen type. Used the velocity coefficient method for the design of the impeller structure.

2.2.1. Impeller Inlet Diameter. This pump is not a through-shaft impeller; instead, it is a cantilever impeller without a hub. Impeller inlet diameter is calculated according to the following equation:

$$D_1 = k_0 k_1 \sqrt[3]{\frac{Q}{n}}, \tag{8}$$

where coefficient $k_0 = 3.6$. And the coefficient k_1 is generally taken as 0.7~1.0, this is determined by the specific rotation number, the lower ratio speed takes the larger value, so take 0.9 here. Finally, $D_1 = 72$ mm.

2.2.2. Impeller Outlet Diameter. Impeller outlet diameter D_2 is calculated according to the following formula:

$$D_2 = k_D \sqrt[3]{\frac{Q}{n}},$$

$$k_D = 9.35 k_{D_2} \left(\frac{n_s}{100}\right)^{-1/2}. \tag{9}$$

The selection of k_{D_2} is related to the form of the pump and the specific speed, so $k_{D_2} = 1.075$ in this paper. After calculation: $D_2 = 291.2$ mm. After rounding, take $D_2 = 295$ mm.

2.2.3. Impeller Outlet Width.
Impeller outlet width b_2 is calculated according to the following formula:

$$b_2 = k_b \sqrt[3]{\frac{Q}{n}},$$

$$k_b = 0.64 k_{b_2} \left(\frac{n_s}{100}\right)^{5/6},$$

(10)

where $k_{b_2} = 1.34$. After calculation: $b_2 = 11.2$ mm.

2.2.4. Other Data Selection.
Blade linear selection of logarithmic spiral, blade inlet angle β_1 is 19°, blade outlet angle β_2 is 33°, blade wrap angle φ is 123°, and blade thickness select 4 mm [24, 25].

2.2.5. Blade Number.
The number of blades is calculated according to the following equation:

$$Z = 6.5 \frac{D_2 + D_1}{D_2 - D_1} \sin \frac{\beta_1 + \beta_2}{2}.$$

(11)

Take the values of D_1, D_2, β_1, and β_2 into calculation and get $Z = 4.732$, so we take $Z = 5$.

2.3. Determination of Volute Size.
The volute is one of the overflow components that transform energy. The shape of the volute has no significant effect on performance and select rectangle here. The main dimensions of the volute are designed as follows:

(1) Base circle diameter D_3

To make the flow channel smooth, usually taken as follows:

$$D_3 = (1.03 \sim 1.08) D_2.$$

(12)

The coefficient for low-specific speed-pumps should be lower. So we take $D_3 = 305$ mm

(2) Volute inlet width b_3

Volute inlet width is determined by considering the 8th cross-section; therefore we try to make the geometry of the 8th cross-section reasonable.

$$b_3 = b_2 + (5 \sim 10).$$

(13)

After calculation: $b_3 = 20$ mm

(3) Setting angle of the volute tongue φ_0

Based on factory experience, take $\varphi_0 = 15°$ in this paper

(4) Area of each cross-section

TABLE 2: Section area table.

Section	1	2	3	4	5	6	7	8
Wrap angle (°)	45	90	135	180	225	270	315	360
Area (mm²)	170.4	340.8	511.1	681.5	851.9	1022.3	1192.6	1363

We use the speed coefficient method for similar conversions as follows:

$$v_3 = k_3 \sqrt{2gH},$$

(14)

where v_3−the average speed of each section; k_3−Speed coefficient, we take 0.46 here.

After calculation: $v_3 = 10.19$ m/s.

The flow through section 8 is nearly equal to the actual flow. Therefore, the area of the 8th section can be calculated by the following formula:

$$F_8 = \frac{Q}{v_3}.$$

(15)

Other section areas are calculated at equal speeds in each section.

$$F_\varphi = \frac{\varphi}{360} F_8.$$

(16)

The area of each section is obtained as follows Table 2:

3. Numerical Simulation

3.1. Computational Model.
Construct the water body parts of the suction section, impeller, and volute. To ensure adequate flows, reduce the influence of the inlet section on the water flow, so it is necessary to increase the length of the inlet section appropriately. The calculation model is shown in Figure 1.

3.2. Determination of the Turbulence Model and Boundary Conditions.
In CFD flow field calculation, the accuracy of the computational model has a decisive influence on the results of the flow field simulation. Commonly, the $k - \varepsilon$ model and $k - \omega$ model have a wide range of applications. The RNG $k - \varepsilon$ model is derived from a rigorous statistical technique, considered turbulent vortex formation, fully investigated the low Reynolds number flow viscosity calculation, and is more suitable for flow in the near wall area. This model is chosen in this paper [26, 27]. The specific expression is shown in the following equation:

$$\begin{cases} \dfrac{\partial(\rho k)}{\partial t} + \dfrac{\partial(\rho k u_i)}{\partial x_i} = \dfrac{\partial}{\partial x_j}\left[\alpha_k \mu_{eff}\dfrac{\partial k}{\partial x_j}\right] + P_k - \rho\varepsilon, \\ \\ \dfrac{\partial(\rho\varepsilon)}{\partial t} + \dfrac{\partial(\rho\varepsilon u_i)}{\partial x_i} = \dfrac{\partial}{\partial x_j}\left[\alpha_\varepsilon \mu_{eff}\dfrac{\partial\varepsilon}{\partial x_j}\right] + C_{1\varepsilon}\dfrac{\varepsilon}{k}P_k - C_{2\varepsilon}\dfrac{\varepsilon^2}{k}\rho. \end{cases}$$
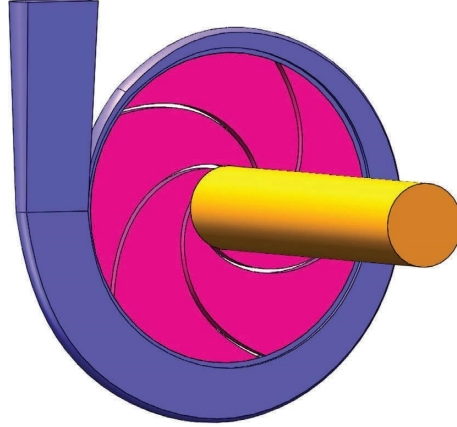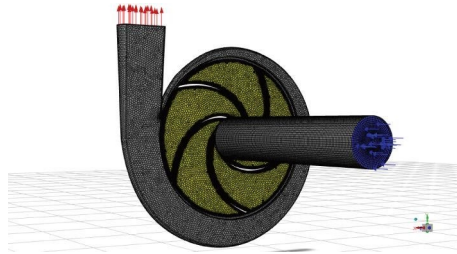
(17)

In the formula

Figure 1: Flow field diagram.

Figure 2: Boundary condition setting diagram.

$$\mu_{\text{eff}} = \mu + \mu_t,$$

$$\mu_t = \rho C_\mu \frac{k^2}{\varepsilon}, \tag{18}$$

where $C_\mu = 0.0845$; $\alpha_k = \alpha_\varepsilon = 1.39$; $C_{1\varepsilon} = 1.42$; $C_{2\varepsilon} = 1.68$.

The mesh file displayed in FLUENT is shown in Figure 2. Inlet boundary selection speed inlet: set the value to 2.76 m/s. Outlet boundary selection mass flow rate: the flow rate is set to 13.89 kg/s. The rotational speed is set to 1440 r/min. Set the impeller blades and back and forward cover plates to the rotating wall; the values are 0 rev/min. Set the shear condition of the static wall to a no-slip wall [28].

3.3. Mesh. In numerical simulations, there are often various factors that affect the final results [29, 30]. To ensure the accuracy of the numerical calculation, it needs to ensure high quality in the near-wall region to enable capture of the flow in the boundary layer, as in Figure 3. Uses y^+ to denote the dimensionless distance from the center of mass of the grid nearest the wall to the wall, the defining equation is as follows:

$$y^+ = \frac{\Delta y u_\tau}{\nu}, \tag{19}$$

where Δy is the distance from the first layer mass center of the mesh to the wall, u_τ is friction velocity, and ν is kinematic viscosity.

In the numerical simulations, the calculated y^+ is shown in Figure 4. Basically around $10 \sim 140$. The requirement of the RNG $k - \varepsilon$ model is $0 \sim 300$, meets the near-wall mesh quality requirements [31].

To ensure the mesh numbers have no effect on the calculation results, get 5 different numbers of meshes. The mesh irrelevance analysis is shown in Table 3. As shown in the table, with the number of meshes increasing, the effect of quantity on the calculation results can be ignored. The finalized mesh number is 3391623. However, the calculation of the hydraulic efficiency requires the measurement of the moment M at the pump shaft, as shown in the following equation:

$$\eta = \frac{\rho g Q H}{M \omega}. \tag{20}$$

3.4. Flow Field Analysis. Simulation of centrifugal pump rated conditions, the result is shown in Figure 5. The simulated head value is 25.470 m, slightly higher than the expected target; this is because leakage losses are not considered.

Figure 6 shows the pressure nephogram of the centrifugal pump. It can be seen that the pressure in the flow path inside the impeller increases gradually along the flow direction, which is the positive pressure gradient. There is a significant pressure difference between the pressure face and the suction face. At an impeller of the same radius, the pressure on the pressure surface is higher than the suction
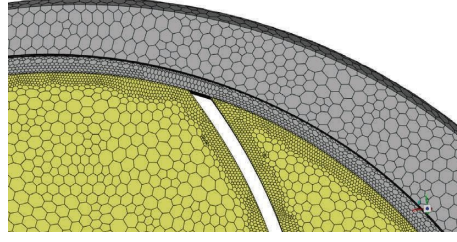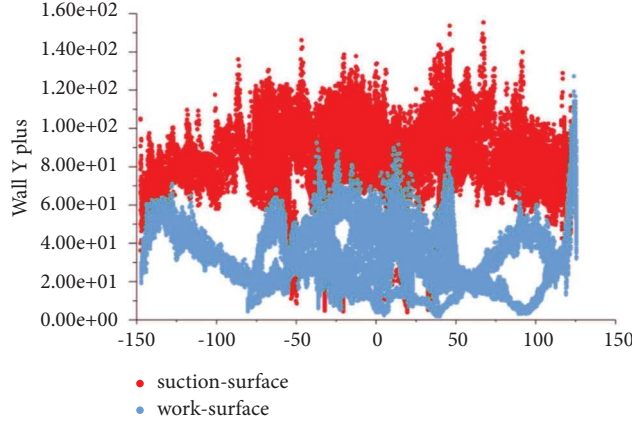
Figure 3: Boundary layer mesh diagram.

Figure 4: y^+ diagram of the impeller boundary.

Table 3: Mesh independence check.

Program number	Scheme 1	Scheme 2	Scheme 3	Scheme 4	Scheme 5
Mesh number	1810458	2554012	3391623	4719423	6238245
Head (m)	25.026	25.035	25.470	25.527	25.467
Hydraulic efficiency (%)	73.91	73.26	72.55	72.73	72.66
Total efficiency (%)	61.46	60.93	60.35	60.50	60.41

surface. At the intersection of the impeller channel and volute base circle, small low-pressure areas appear; this is a direct result of diffusion at the channel outlet of the low-specific speed pump. The model has a good pressure distribution that is consistent with reality.

Figure 7 shows the velocity streamlines of the flow field. The lower velocity region occupies most of the blade's working surface in the figure, and backflow occurs throughout the middle channel, only away from the volute tongue can be slightly relieved. Backflow causes channel blockage and consumes large amounts of fluid kinetic energy, decreasing the performance of centrifugal pumps.

The Reynolds number is usually used to determine the flow state of viscous fluids; it means the ratio of the inertial force to the viscous force. The ideal flow state inside the impeller is a steady laminar flow along the channel. But as the flow progresses to the trailing edge, the Reynolds number increases, the thickness of the laminar boundary layer gradually thickens, and flow disturbances begin to develop. When creating coordinates, set along the impeller from the inlet to the outlet direction as the positive direction of the x-axis, the vertical direction of the blade is set as the positive direction of the y-axis, assumed constant incompressible fluid, the $N - S$ equation is

$$
\begin{cases}
\dfrac{\partial u}{\partial x} + \dfrac{\partial v}{\partial y} = 0, \\[2ex]
u\dfrac{\partial u}{\partial x} + v\dfrac{\partial u}{\partial y} = -\dfrac{1}{\rho}\dfrac{\partial p}{\partial x} + v\left(\dfrac{\partial^2 u}{\partial x^2} + \dfrac{\partial^2 u}{\partial y^2}\right), \\[2ex]
u\dfrac{\partial v}{\partial x} + v\dfrac{\partial v}{\partial y} = -\dfrac{1}{\rho}\dfrac{\partial p}{\partial y} + v\left(\dfrac{\partial^2 v}{\partial x^2} + \dfrac{\partial^2 v}{\partial y^2}\right).
\end{cases}
\tag{21}
$$

Ignoring smaller magnitudes, simplify equation (21) to

$$
\frac{\partial u}{\partial x} + \frac{\partial v}{\partial y} = 0,
\tag{22a}
$$

$$
u\frac{\partial u}{\partial x} + v\frac{\partial u}{\partial y} = -\frac{1}{\rho}\frac{\partial p}{\partial x} + v\frac{\partial^2 u}{\partial y^2},
\tag{22b}
$$

(a)   (b)
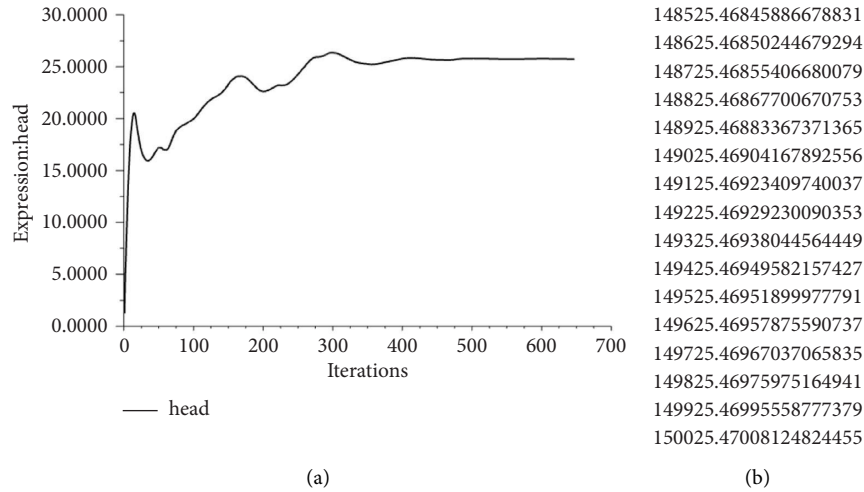
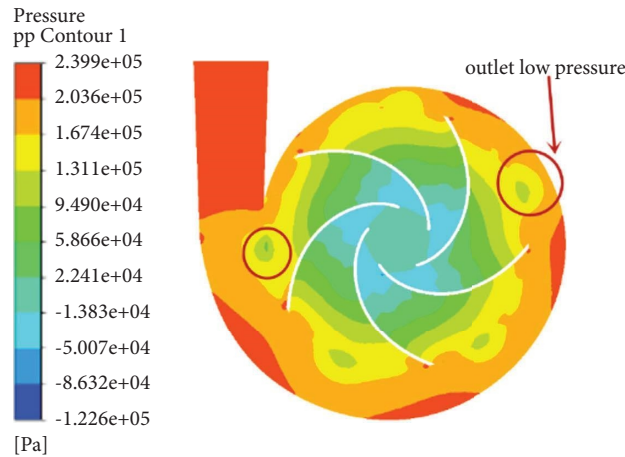Figure 5: Diagram of head simulation. (a) Head curve diagram. (b) Head monitoring documentation diagram.

Figure 6: Pressure nephogram.

$$0 = \frac{\partial p}{\partial y}. \tag{22c}$$

From equation (22c), we can get the following result: the pressure p of the fluid boundary layer does not change along the y direction. This indicates that the fluid disturbance is caused by a pressure change in the x-axis direction: during flow channel diffusion, there is a negative pressure gradient in the x-axis direction, that is, $\partial p / \partial x < 0$ in equation (22b). When the pressure is less than the resistance during flow and the flow direction changes, turbulence begins to develop.

From a macro perspective, in the flow channel between two blades, the differential pressure between the back and working surface is high pressure and low speed at the working surface, meanwhile, the opposite is shown for the suction surface. This pressure gradient forces the fluid to flow towards the back of the blade, which will create secondary flows and increase flow losses. With integrated consideration of boundary layer control methods and low-specific-speed centrifugal pump internal flow conditions,

this paper uses slit blades to improve the performance of centrifugal pumps.

4. Experimental Design and Results Analysis

4.1. Orthogonal Experimental Design. There are many geometric parameters of the slotted blade, and with a balance between the number of experiments and the mastery of experimental rules, an orthogonal experiment of 5 factors and 4 levels for analysis was designed. According to the characteristics of the flow channel and the structure of the blade, decided to select the factors as the diameter of slit D, slit center width b, deflection angle of slit β, depth of slit h, shrinkage ratio of slit f, and denoted by A, B, C, D, E in order. Where the shrinkage ratio f is defined as the ratio of the width of the slit at the pressure surface to the width of the slit at the suction surface. The parameters are defined in Figure 8.

In order for the slit to act directly on the low-velocity backflow area and effectively improve the performance: Slits
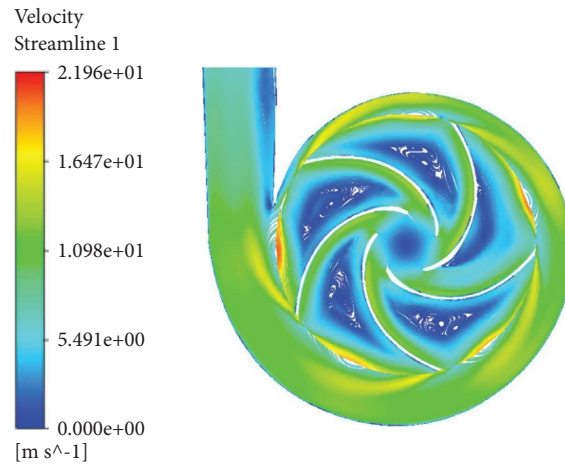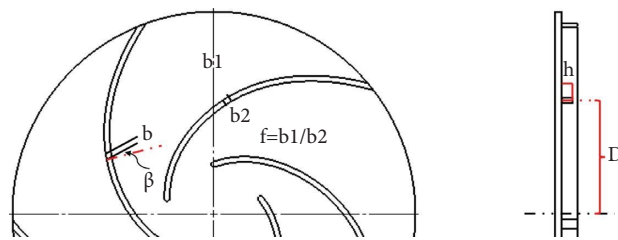
FIGURE 7: Velocity streamlines of the flow field.

FIGURE 8: Slit geometry parameters.

TABLE 4: Factor and level table.

| Level | Factor | | | | |
	Diameter of slit D (mm)	Slit center width b (mm)	Deflection angle of slit β (°)	Depth of slit h (mm)	Shrinkage ratio of slit f
1	136	2	20	2	0.5
2	168	3	50	4	0.8
3	200	2.3	−20	6	1.2
4	232	2.7	−50	8	1.5

will be set in areas of severe backflow, and 4 slit positions will be evenly selected. Meanwhile, to investigate the effect of different slit shapes, other factors were also selected at 4 levels based on blade size. Based on the selected factors and levels, select $L_{16}(4^5)$ orthogonal table. The specific values are shown in Table 4.

Part of the slit shape is shown in Figure 9. The figure shows the fluid field with the presence of slits.

Table 5 shows the calculation results of 16 orthogonal tests at the rated flow rate.

4.2. Process and Analysis of Experimental Results

4.2.1. Direct Analysis. Figure 10 shows the results of 16 groups of orthogonal tests, the specific parameters are shown in Table 5.

Visual analysis by Figure 10: the effect on pump performance is very significant after opening the blade

slits, and the factors influence and constrain each other. The shape of the slit with the highest head is the 16th group, at 25.859 m, up 0.389 m over the original model. Group 11 is the most efficient, 60.78%, up 0.43% over the original model. Additionally, the group 13 model head reduction was 0.598 m, and the efficiency dropped by 1.86%. It can be seen that the unreasonable shape of the slit can seriously damage the performance of the centrifugal pump.

The flow field of these centrifugal pumps is shown in Figure 11. As seen by this, a proper slit shape (e.g., group 11, group 16) will significantly compress the backflow area of the flow channel, reduce the internal consumption of fluid kinetic energy, and increase the head and efficiency of centrifugal pumps. An unreasonable slit shape (group 13) will cause fluid of the pressure surface through the slit to neither improve the fluid exit velocity triangle nor destroys the backflow structure at the end of the flow
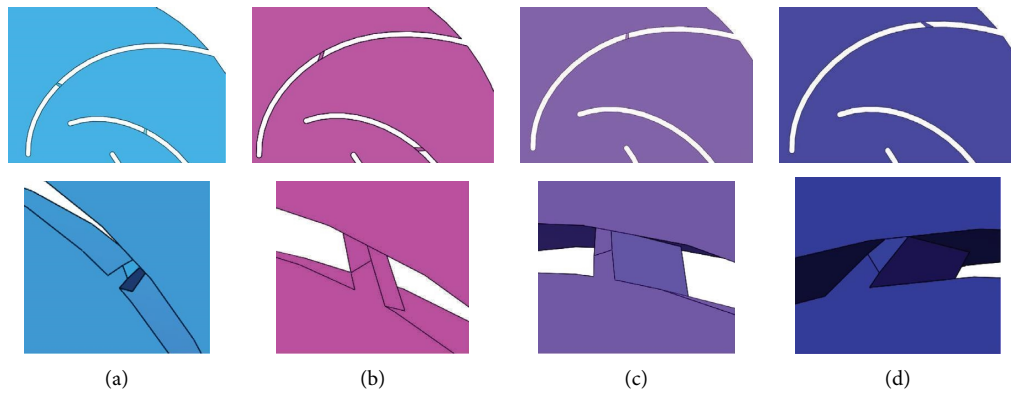
FIGURE 9: Slit watershed shape diagram: (a) Group 1; (b) Group 7; (c) Group 9; (d) Group 15.

TABLE 5: Orthogonal experiment data table.

Number	A	B	C	D	E	Total efficiency η%	Head H (m)
1	136	2	20	2	0.5	60.82	25.490
2	136	3	50	4	0.8	60.29	25.337
3	136	2.3	−20	6	1.2	59.54	25.475
4	136	2.7	−50	8	1.5	59.06	25.517
5	168	2	50	6	1.5	60.40	25.340
6	168	3	20	8	1.2	59.87	25.464
7	168	2.3	−50	2	0.8	60.54	25.415
8	168	2.7	−20	4	0.5	60.40	25.396
9	200	2	−20	8	0.8	60.28	25.682
10	200	3	−50	6	0.5	60.74	25.598
11	200	2.3	20	4	1.5	60.78	25.483
12	200	2.7	50	2	1.2	60.39	25.347
13	232	2	−50	4	1.2	58.49	24.872
14	232	3	−20	2	1.5	60.30	25.422
15	232	2.3	50	8	0.5	59.85	25.120
16	232	2.7	20	6	0.8	60.30	25.859
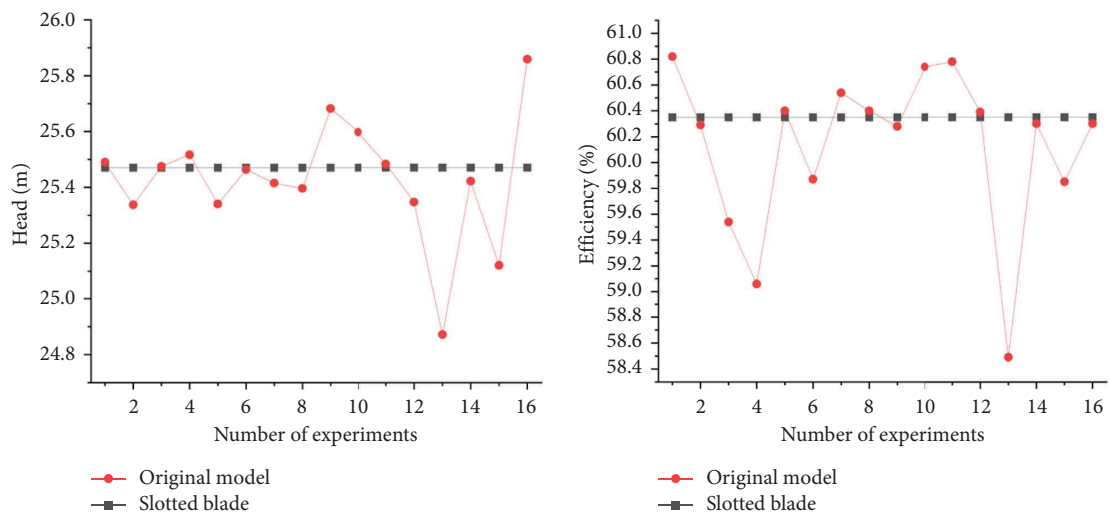
FIGURE 10: Orthogonal test results figure.

Velocity
body
2.223e+01
1.667e+01
1.112e+01
5.558e+00
0.000e+00
[m s^-1]

(a) Velocity vector diagram

group 11

(b) Pressure Diagram

(c) Speed Flow Diagram

(d) Partial diagram

Velocity
body
2.538e+01
1.903e+01
1.269e+01
6.344e+00
0.000e+00
[m s^-1]

(a) Velocity vector diagram

group 13

(b) Pressure Diagram

(c) Speed Flow Diagram

(d) Partial diagram

Velocity
body
2.221e+01
1.666e+01
1.110e+01
5.552e+00
0.000e+00
[m s^-1]

(a) Velocity vector diagram

group 16

(b) Pressure Diagram

(c) Speed Flow Diagram

(d) Partial diagram

FIGURE 11: Flow field diagram of each model.

TABLE 6: Extreme difference analysis of head.

Index	Factor				
	A	B	C	D	E
K_1	101.819	101.384	102.296	101.674	101.604
K_2	101.615	101.821	101.144	101.088	102.293
K_3	102.11	101.493	101.975	102.272	101.158
K_4	101.273	102.119	101.402	101.783	101.762
$\overline{K_1}$	25.45475	25.346	25.574	25.4185	25.401
$\overline{K_2}$	25.40375	25.45525	25.286	25.272	25.57325
$\overline{K_3}$	25.5275	25.37325	25.49375	25.568	25.2895
$\overline{K_4}$	25.31825	25.52975	25.3505	25.44575	25.4405
Optimal level	3	4	1	3	2
R	0.20925	0.18375	0.288	0.296	0.28375
Order	4	5	2	1	3

TABLE 7: Extreme difference analysis of efficiency.

Index	Factor				
	A	B	C	D	E
K_1	239.71	239.99	241.77	242.05	241.81
K_2	241.21	241.2	240.93	239.96	241.41
K_3	242.19	240.71	240.52	240.98	240.98
K_4	238.94	240.15	238.83	239.06	240.54
$\overline{K_1}$	59.9275	59.9975	60.4425	60.5125	60.4525
$\overline{K_2}$	60.3025	60.3	60.2325	59.99	60.3525
$\overline{K_3}$	60.5475	60.1775	60.13	60.245	60.245
$\overline{K_4}$	59.735	60.0375	59.7075	59.765	60.135
Optimal level	3	2	1	1	1
R	0.8125	0.3025	0.735	0.7475	0.3175
Order	1	5	3	2	4

R is the extreme difference value in the table, the larger the value, indicates that the greater the influence of the factor on the index.

channel. Instead, the backflow is locally enhanced by the blowing effect, which causes degradation of centrifugal pump performance.

4.2.2. Extremum Difference Analysis. In order to investigate the influence degree of each factor on the performance of the flow field, do an extreme difference analysis for head and efficiency, respectively, the results are shown in Tables 6 and 7.

For the head, changes in factor C (deflection angle of slit β) and factor D (depth of slit h) have a greater effect on the head, and factor B (slit center width b) has a small effect on the head by changing. The order of impact from largest to smallest is $D > C > E > A > B$. The optimal combination of the head is $A_3B_4C_1D_3E_2$.

For efficiency: factor A (diameter of slit D) has a large effect on the variation of efficiency, while factor B (slit center width b) and factor E (shrinkage ratio of slit f) have a small effect on the efficiency. The order of impact from largest to smallest is $A > D > C > E > B$. The optimal combination for efficiency is $A_3B_2C_1D_1E_1$.

5. Multiobjective Optimization Based on Entropy Weight TOPSIS

5.1. Analysis of Entropy Weight TOPSIS. Direct extreme difference analysis for a single target only. To fully judge the performance indicators of centrifugal pumps, we need to transform multiobjective problems into single-objective problems through empowerment to facilitate a comprehensive evaluation of pump performance. The entropy weighting method determines the weights by the entropy value of each index. The weight coefficients are calculated as follows:

(1) Constructs the head and efficiency from the orthogonal test results as a decision matrix of $X_{m \times n}$ as shown in the following equation:

$$X_{m \times n} = \begin{bmatrix} x_{11} & x_{12} & \cdots & x_{1n} \\ x_{21} & x_{22} & \cdots & x_{2n} \\ \cdots & \cdots & \cdots & \cdots \\ x_{m1} & x_{m2} & \cdots & x_{mn} \end{bmatrix}, \quad (23)$$

where m—Number of experiments; n—Number of test indexes.

(2) To facilitate comparison of results, regularization is performed according to the following equation:

$$\lambda_{ij} = \frac{x_{ij}}{\sqrt{\sum_{i=1}^{m} x_{ij}^2}}, \tag{24}$$

where λ_{ij}—Regularization results of the j indicators in the number i test.

(3) Calculate the weight of the sum of test values for the i th value under the j th indicator.

$$p_{ij} = \frac{\lambda_{ij}}{\sum_{i=1}^{m} \lambda_{ij}}. \tag{25}$$

(4) Calculate the entropy value of each index.

$$e_j = -k \sum_{i=1}^{m} p_{ij} \ln(p_{ij}), \tag{26}$$

where k—$1/\ln(m)$.

(5) Calculate the information entropy redundancy of each index.

$$d_j = 1 - e_j. \tag{27}$$

(6) Calculate the weighting coefficients of each index.

$$\omega_j = \frac{d_j}{\sum_{j=1}^{n} d_j} \times 100\%. \tag{28}$$

Bringing the results of the orthogonal tests into equations (26) to (28) in turn, the weights of efficiency and head were obtained as 60.08% and 39.92%. Through the TOPSIS method, we ranked the 16 sets of experimental results according to their proximity to the idealized target to evaluate their relative merits. The calculation steps are as follows:

(1) We create a weighting matrix as follows:

$$Z = [z_{ij}] = \begin{bmatrix} z_{11} & \cdots & z_{1n} \\ \vdots & \ddots & \vdots \\ z_{m1} & \cdots & z_{mn} \end{bmatrix}, \tag{29}$$

where $i = 1, 2, 3, \cdots, m$; $j = 1, 2, , \cdots, n$; and $z_{ij} = \lambda_{ij} \times \omega_j$.

(2) To find the optimal and inferior solutions we use the following equations:

$$\begin{aligned} z_{ij}^+ &= \max_{m,n} (z_1^+, z_2^+, \cdots, z_m^+), \\ z_{ij}^- &= \min_{m,n} (z_1^-, z_2^-, \cdots, z_m^-). \end{aligned} \tag{30}$$

(3) To calculate the distance between the evaluation object and the optimal/inferior solutions we use the following equation:

$$\begin{aligned} D_i^+ &= \sqrt{\sum_j (z_{ij} - z_j^+)^2}, \\ D_i^- &= \sqrt{\sum_j (z_{ij} - z_j^-)^2}. \end{aligned} \tag{31}$$

(4) To calculate the relative proximity of the evaluation object to the optimal state we use the following equation:

$$C_i = \frac{D_i^-}{D_i^+ + D_i^-}. \tag{32}$$

Finally, ranking according to the value of C_i. The larger the C_i is the closer the evaluation object to the optimal state. The evaluation results are shown in Table 8.

Obtained from Table 8, with the balance of head and efficiency, the shape of the slit in the 10th group is optimal: its efficiency rises by 0.39% compared to the original model, the head rises by 12.8cm, and both indicators have improved significantly.

5.2. Multiobjective Optimization. In order to get the optimal level that takes into account head and efficiency, we can perform an extreme variance analysis on the weighted index. The results are shown in Table 9.

With a compromise between efficiency and head, the optimal combination is: $A_3 B_2 C_1 D_3 E_1$; that is, the diameter of the slit D is 200 mm, the slit center width b is 3 mm, the deflection angle of the slit β is $-20°$, depth of the slit h is 6 mm, and the shrinkage ratio of the slit f is 0.5. Performed hydraulic performance simulations on the optimized slotted impeller geometry parameters, its efficiency rises by 0.32% compared to the original model, the head rises by 0.113m, proven to have some optimization effect. Its flow channel pressure nephogram is shown in Figure 12, the velocity streamline diagram is shown in Figure 13.

By optimizing the structural parameters of low-specific-speed centrifugal pumps, we compare the optimization results and obtain Table 10.

5.3. Experimental Verification. To verify the reasonableness and reliability of the slotted blade, conduct physical experiments on the model. 3D printed the overcurrent parts used, as shown in Figure 14.

Assemble the closed pump performance test bench to completion, as shown in Figure 15.

Underrated conditions (1440 r/min; 50 m³/h⁻¹), we conducted several hydraulic performance tests on the original model blade and the optimized one, and the obtained results were taken as the mean value. The original model head is 24.13 m, after optimization, the head is 24.58 m. After measuring the moment M of the pump shaft by the parameters measurement instrument. The total

TABLE 8: TOPSIS evaluation results.

Number of tests	Positive ideal solution distance D_i^+	Negative ideal solution distance D_i^-	Relative proximity C_i	Rank
1	0.147	1.421	0.906	2
2	0.381	1.097	0.742	11
3	0.784	0.675	0.463	14
4	1.066	0.428	0.287	15
5	0.326	1.163	0.781	7
6	0.592	0.862	0.593	12
7	0.244	1.251	0.837	4
8	0.313	1.166	0.789	5
9	0.332	1.123	0.772	9
10	0.115	1.382	0.923	1
11	0.152	1.397	0.902	3
12	0.329	1.157	0.778	8
13	1.454	0	0	16
14	0.358	1.109	0.756	10
15	0.653	0.823	0.558	13
16	0.312	1.157	0.787	6

TABLE 9: Weighted index extreme deviation table.

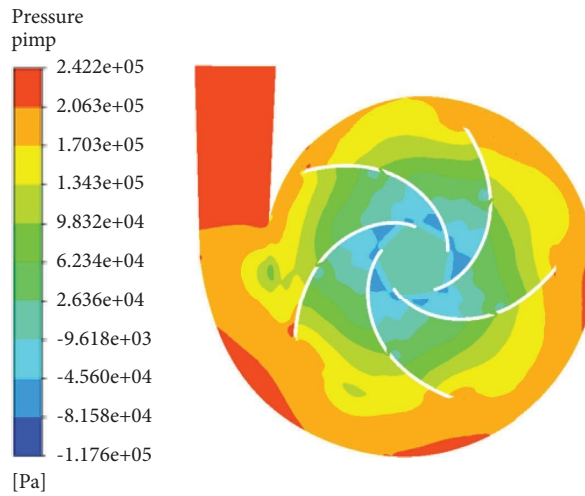| Index	Factor				
	A	B	C	D	E
$\overline{K_1}$	46.16598	46.16462	46.52299	46.40298	46.45994
$\overline{K_2}$	46.37092	46.38998	46.28186	46.13057	46.46862
$\overline{K_3}$	46.56752	46.28364	46.30321	46.50194	45.88673
$\overline{K_4}$	45.99583	46.26201	45.99219	46.06476	46.28496
Optimal level	3	2	1	3	1

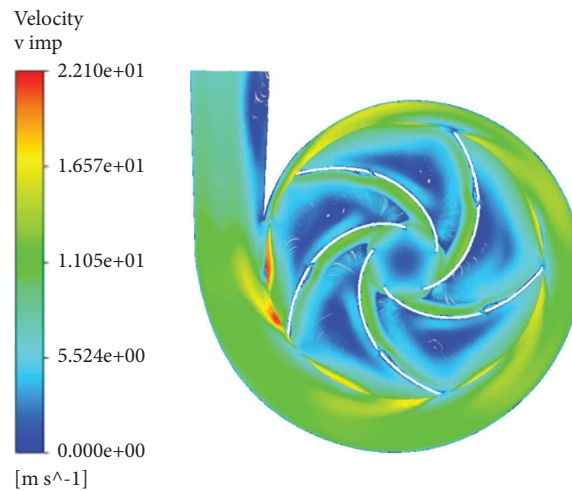
FIGURE 12: Optimized pressure nephogram.

Figure 13: Optimized velocity streamlines.

Table 10: Comparison of optimization results.

Index	Rank	Parameter combinations	Efficiency (%)	Head (m)
Original model	—	—	60.35	25.470
Optimal efficiency	A > D > C > E > B	$A_3B_2C_1D_1E_1$	60.85	25.410
Optimal head	D > C > E > A > B	$A_3B_5C_1D_3E_2$	60.35	25.870
Multiobjective	B > A > E > D > C	$A_3B_2C_1D_3E_1$	60.67	25.583

(a)   (b)

Figure 14: Overcurrent parts figure (a) impeller and (b) volute.

(a)

(b)

FIGURE 15: Closed pump performance test bench diagram: (a) front view and (b) lateral view.

efficiency of the test system is calculated using equation (32). The original model efficiency was 55.33%, and the efficiency after optimization was 57.82%. There was a good performance enhancement effect.

$$\eta = \frac{\rho g Q H}{1000 U I}. \qquad (33)$$

6. Conclusions and Foresights

6.1. Conclusions

(1) Simulated the flow field of a low-specific-speed centrifugal pump and analyzed the reasons for the inefficiency. Low-specific-speed pump flow channel outlet diffusion is serious, and there is a pressure gradient between the back of the blade and the working surface, which generates extremely large backflow areas, causes blockage of flow channels, and consumes large amounts of fluid kinetic energy.

(2) Designed the $L_{16}(4^5)$ orthogonal table, and conducted orthogonal experiments on the impeller slit geometry parameters. The optimal combination of geometric parameters for the head is $A_3B_4C_1D_3E_2$, that is, the diameter of slit D is 200 mm, slit center width b is 2.7 mm, the deflection angle of slit β is 20°, depth of slit h is 6 mm, shrinkage ratio of slit f is 0.8. The ranking of impacts from largest to smallest is the depth of slit h > deflection angle of slit β > shrinkage ratio of slit f > diameter of slit D > slit center width b

The optimal combination of efficiency is: $A_3B_2C_1D_1E_1$, that is, the diameter of slit D is 200 mm, slit center width b is 3 mm, the deflection angle of slit β is 20°, depth of slit h is 2 mm, shrinkage

ratio of slit f is 0.5. The importance is the diameter of slit D > depth of slit h > deflection angle of slit β > shrinkage ratio of slit f > slit center width b.

The combination of slit geometry parameters that take into account both head and efficiency is $A_3B_2C_1D_3E_1$, that is, the diameter of slit D is 200 mm, slit center width b is 3 mm, the deflection angle of slit β is 20°, depth of slit h is 6 mm, shrinkage ratio of slit f is 0.5. The order of effects is: slit center width b > diameter of slit D > shrinkage ratio of slit f > depth of slit h > deflection angle of slit β.

(3) Performed simulation of the optimized model by FLUENT, the obtained head and efficiency are 25.583 m and 60.67%, respectively, which is an improvement over the original model. Verified through experiments that the hydraulic performance has indeed improved. It is concluded that the entropy power TOPSIS method is useful for the optimization of structural parameters of centrifugal pumps.

6.2. Foresights. Improvements in centrifugal pump performance mean progress for the entire drainage and water supply industries. Based on the above conclusions, further research may be conducted on the following aspects:

(1) In this paper, the flow field state at the cross-section of the slit is observed. We could select multiple cross-sections to describe the flow field of the slit blade in more detail.

(2) In this paper, four representative levels of each factor were selected. Researchers could do this by numerical twinning, etc., to obtain a more accurate hydraulic model.

Data Availability

The data used to support the findings of this study are included within the article.

Conflicts of Interest

The authors declare that there are no conflicts of interest regarding the publication of this paper.

Authors' Contributions

Conceptualization was carried out by Ke Qidi and Tang Lingfeng; methodology was carried out by Ke Qidi; software development was looked after by Ke Qidi; validation was given by Ke Qidi and Tang Lingfeng; formal analysis was conducted by Tang Lingfeng; the investigation was carried out by Ke Qidi; resources were collected by Ke Qidi; data curation was carried out by Ke Qidi; writing—original draft preparation was done by Ke Qidi; writing—review and editing was done and visualized by Ke Qidi; supervision project administration and funding acquisition were done by Tang Lingfeng.

References

[1] N. Pokharel, A. Ghimire, B. Thapa, and B. S. Thapa, "Wear in centrifugal pumps with causes, effects and remedies: a Review," *IOP Conference Series: Earth and Environmental Science*, vol. 1037, no. 1, Article ID 12042, 2022.

[2] X. B. Chen, R. H. Zhang, and W. F. J. J. O. A. F. M. Yang, "Inverse design and optimization of low specific speed centrifugal pump blade based on adaptive POD hybrid model [J]," *Journal of Applied Fluid Mechanics*, vol. 10, 2022.

[3] W. Xiao and L. Tan, "Design method of controllable velocity moment and optimization of pressure fluctuation suppression for a multiphase pump," *Ocean Engineering*, vol. 220, Article ID 108402, 2021.

[4] R. De Donno, A. Ghidoni, G. Noventa, and S. J. O. Rebay, "Shape optimization of the ERCOFTAC centrifugal pump impeller using open-source software," *Optimization and Engineering*, vol. 20, no. 3, pp. 929–953, 2019.

[5] S. Thakkar, H. Vala, V. K. Patel, and R. M. J. J. B. S. O. M. S. Patel, "Performance improvement of the sanitary centrifugal pump through an integrated approach based on response surface methodology, multi-objective optimization and CFD," *Journal of the Brazilian Society of Mechanical Sciences and Engineering*, vol. 43, pp. 24–15, 2021.

[6] A. R. Al-Obaidi and H. J. J. O. A. F. M. Towsyfyan, "An experimental study on vibration signatures for detecting incipient cavitation in centrifugal pumps based on envelope spectrum analysis," *Journal of Applied Fluid Mechanics*, vol. 12, no. 6, pp. 2057–2067, 2019.

[7] A. R. J. E. T. Al-Obaidi, "Detection of cavitation phenomenon within a centrifugal pump based on vibration analysis technique in both time and frequency domains," *Experimental Techniques*, vol. 44, no. 3, pp. 329–347, 2020.

[8] H. Zhang, L. Tang, and Y. Zhao, "Influence of blade profiles on plastic centrifugal pump performance," *Advances in Materials Science and Engineering*, vol. 2020, Article ID 6665520, 17 pages, 2020.

[9] Z. C. Zhang, H. X. Chen, Z. Ma, J. W. He, H. Liu, and C. J. J. O. F. E. Liu, "Research on improving the dynamic performance of centrifugal pumps with twisted gap drainage blades," *Journal of Fluids Engineering*, vol. 141, no. 9, 2019.

[10] L. Bai, L. Zhou, X. Jiang, Q. Pang, and D. J. S. Ye, "Vibration in a multistage centrifugal pump under varied conditions," *Shock and Vibration*, vol. 2019, Article ID 2057031, 9 pages, 2019.

[11] J. Feng, Z. Ge, H. Yang, G. Zhu, C. Li, and X. Luo, "Rotating stall characteristics in the vaned diffuser of a centrifugal pump," *Ocean Engineering*, vol. 229, Article ID 108955, 2021.

[12] H. Stel, E. M. Ofuchi, R. H. G. Sabino et al., "Investigation of the motion of bubbles in a centrifugal pump impeller," *Journal of Fluids Engineering*, vol. 141, no. 3, 2018.

[13] M. Namazizadeh, M. Talebian Gevari, M. Mojaddam, and M. Vajdi, "Optimization of the splitter blade configuration and geometry of a centrifugal pump impeller using design of experiment," *Journal of Applied Fluid Mechanics*, vol. 13, no. 1, pp. 89–101, 2020.

[14] M. Liu, L. Tan, Y. Xu, and S. Cao, "Optimization design method of multi-stage multiphase pump based on Oseen vortex," *Journal of Petroleum Science and Engineering*, vol. 184, Article ID 106532, 2020.

[15] Y. Lu, L. Tan, Y. Han, and M. Liu, "Cavitation-vibration correlation of a mixed flow pump under steady state and fast start-up conditions by experiment," *Ocean Engineering*, vol. 251, Article ID 111158, 2022.

[16] M. Liu, L. Tan, and S. J. F. I. E. R. Cao, "Performance prediction and geometry optimization for application of pump as turbine: a review," *Frontiers in Energy Research*, vol. 9, Article ID 818118, 2022.

[17] J. Li, R. Zhang, H. Xu, and J. Feng, "Two-stage design optimization of groove flow control technique to improve energy performance of an axial-flow pump," *Journal of the Brazilian Society of Mechanical Sciences and Engineering*, vol. 44, no. 8, p. 381, 2022.

[18] N. Zhang, X. Liu, B. Gao, and B. Xia, "DDES analysis of the unsteady wake flow and its evolution of a centrifugal pump," *Renewable Energy*, vol. 141, pp. 570–582, 2019.

[19] H. Wang, B. Long, C. Wang, C. Han, and L. Li, "Effects of the impeller blade with a slot structure on the centrifugal pump performance," *Energies*, vol. 13, no. 7, p. 1628, 2020.

[20] Y. Yang, L. Zhou, H. Zhou et al., "Optimal design of slit impeller for low specific speed centrifugal pump based on orthogonal test," *Journal of Marine Science and Engineering*, vol. 9, no. 2, p. 121, 2021.

[21] Y. Wei, Y. Yang, L. Zhou, L. Jiang, W. Shi, and G. Huang, "Influence of impeller gap drainage width on the performance of low specific speed centrifugal pump," *Journal of Marine Science and Engineering*, vol. 9, no. 2, p. 106, 2021.

[22] L. Zhang, H. Li, H. Xu et al., "Experimental and numerical investigation of pressure fluctuation in a low-specific-speed centrifugal pump with a gap drainage impeller," *Shock and Vibration*, vol. 2021, Article ID 5571178, 14 pages, 2021.

[23] R. h. Zhang, L.-c. Yun, and J. J. J. O. H. Li, "The effect of impeller slot jet on centrifugal pump performance," *Journal of Hydrodynamics*, vol. 31, no. 4, pp. 733–739, 2018.

[24] S. H. Susilo and A. J. E. P. Setiawan, "Analysis of the number and angle of the impeller blade to the performance of centrifugal pump," *Eureka*, vol. 5, pp. 62–68, 2021.

[25] Z. Xu, F.-y. Kong, L. Tang, M. Liu, J. Wang, and N. J. M. Qiu, "Effect of blade thickness on internal flow and performance of a plastic centrifugal pump," *Machines*, vol. 10, 2022.

[26] H. L. Liu, Y. Wang, D. X. Liu, S. Q. Yuan, and J. Wang, "Assessment of a turbulence model for numerical predictions of sheet-cavitating flows in centrifugal pumps," *Journal of Mechanical Science and Technology*, vol. 27, no. 9, pp. 2743–2750, 2013.

[27] A. Ramadhan Al-Obaidi and N. Simulation, "Effects of different turbulence models on three-dimensional unsteady cavitating flows in the centrifugal pump and performance prediction," *International Journal of Nonlinear Sciences and Numerical Stimulation*, vol. 20, no. 3-4, pp. 487–509, 2019.

[28] Y. Gu, J. Li, P. Wang et al., "An improved one-dimensional flow model for side chambers of centrifugal pumps considering the blade slip factor," *Journal of Fluids Engineering*, vol. 144, no. 9, 2022.

[29] O. Babayigit, M. Ozgoren, M. H. Aksoy, and O. J. D. W. T. Kocaaslan, "Experimental and CFD investigation of a multistage centrifugal pump including leakages and balance holes," *Water Treat*, vol. 67, no. 3, pp. 28–40, 2017.

[30] O. Kocaaslan, M. Ozgoren, M. H. Aksoy, and O. Babayigit, "Experimental and numerical investigation of coating effect on pump impeller and volute," *Journal of Applied Fluid Mechanics*, vol. 9, no. 7, pp. 2475–2487, 2016.

[31] Z. Wei, W. Yang, and R. J. S. Xiao, "Pressure fluctuation and flow characteristics in a two-stage double-suction centrifugal pump," *Symmetry*, vol. 11, no. 1, p. 65, 2019.